That is,

$$i\,C_2 + \left\lceil \frac{iT_2}{T_3} \right\rceil C_3 \leq a_1(iT_2)$$

We show next that the inequality

$$(k+1)\,C_2 + C_3 \leq a_1(T_3)$$

implies all inequalities in Inequality (2). Since $i(k+1) \geq [iT_2/T_2]$, the inequality

$$i(k+1)\,C_2 + i\,C_3 \leq i\,a_1(T_3)$$

implies

$$\left\lceil \frac{iT_3}{T_2} \right\rceil C_2 + i\,C_3 \leq i\,a_1(T_3)$$

which in turn implies

$$\left\lceil \frac{iT_3}{T_2} \right\rceil C_2 + i\,C_3 \leq a_1(iT_3)$$

The theorem is proved.

e. Comparison and comment. The constraints developed by Theorems 2 to 4 strongly suggest that 100% utilization is not achievable universally by the mixed scheduling algorithm. The following simple example will illustrate: Let $T_1 = 3$, $T_2 = 4$, $T_3 = 5$, and $C_1 = C_2 = 1$. Since $a_1(20) = 13$, it can be easily seen that the maximum allowable $C_3 = 2$. The corresponding utilization factor is

$$\mu = \frac{1}{3} + \frac{1}{4} + \frac{2}{5} = 98.3\%$$

If these three tasks are scheduled by the deadline scheduling algorithm, C_2 can increase to $2.0833\cdots$ and achieve 100% utilization. If they are all scheduled by the period-driven scheduling algorithm, C_2 is restricted to 1 or less and utilization is restricted to at most

$$\mu = \frac{1}{3} + \frac{1}{4} + \frac{1}{5} = 78.3\%$$

which is only slightly greater than the worst-case three-task utilization bound.

Although a closed-form expression for the least upper bound to processor utilization has not been found for the mixed scheduling algorithm, this example strongly suggests that the bound is considerably less restrictive for the mixed algorithm than for the period-driven algorithm. The mixed algorithm may thus be appropriate for many applications, since it can be implemented via the interrupt hardware of present day computers, and provides most of the capability of the fully deadline-driven algorithm.

B. Communications Elements Research

1. Improved RF Calibration Techniques: System-Operating Noise-Temperature Calibrations of the JPL Research Cones, C. T. Stelzried

The system-operating noise-temperature performance of the low-noise research cones is reported. The operating noise-temperature calibrations are performed with the ambient termination technique (SPS 37-42, Vol. III, pp. 25–32). The principal advantage of this method is the stability and reliability of the ambient termination.

The research cones using this operational technique during this reporting period are:

(1) S-band planetary radar (SPR) cone.

(2) S-band research operational (SRO) cone.

(3) S-band cassegrain ultra (SCU) cone.

These cones are operated at the DSS 13 and 14 antennas in a cassegrain configuration.[1] The calibration parameters of the JPL research cones are summarized in Table 7.

The averaged operating noise-temperature calibrations were taken for the various research cone configurations during the period June 1 through October 1, 1969. The various cases are defined in Table 8. The calibrations are presented in Table 9. The data taken at DSS 14 with maser 2 (cases 7 and 8) used an aperture load placed in position by hand over the horn opening.

The operating noise-temperature data were reduced with JPL computer program ID 5841000, CTS 20B. The indicated errors in Table 9 are the standard deviation of the individual measurements and of the means, and

[1]The calibration data were taken by Goldstone DSCC personnel at the stations indicated.

Table 7. Calibration parameters of the JPL research cones

Cone			Construction date	Frequency, MHz	Maser		Noise box correction, dB		VSWR[c]			Approximate zenith low-noise path operating noise temperature, °K		Comments
Model	SN	Mod			SN	Temperature, °K	C_1 (gain)[a]	C_2 (VSWR)[b]	S_A	S_e	S_P	Ground-located	Antenna-mounted	
SPR	01	02	5/68	2295		5.3	26.0	20.0	1.250	1.174	1.280			SPS 37-53, Vol. II, pp. 87–90
				2388		5.0	26.0	20.0	1.084	1.463	1.020	17.5	21.0	
SRO	01	00	7/69	2295	02	5.3	33.0	33.0	1.020	1.174	1.128		18.8	SPS 37-56, Vol. II, pp. 110–113
				2388		5.0	33.0	33.0	1.040	1.463	1.010		17.1	
SCU	01	02	6/69	2297	05	4.2	33.0	33.0	1.061	1.135	1.001	13.1	16.9	SPS 37-58, Vol. II, pp. 55–56
				2388		4.2	33.0	33.0	1.130	1.300[d]	1.081		22.6	
SCU (3A)				2297	03	5.5	33.0	33.0	1.004	1.135	1.003		22.1	
				2388		5.5	33.0	33.0	1.284	1.300[d]	1.292			

[a] C_1 = Path loss to maser input referenced to maser output.

[b] C_2 = Path loss to maser input referenced to termination or antenna under evaluation.

[c] S_A, S_e, S_P = VSWR, defined at maser input, of antenna (right-handed circular polarization), maser input, and ambient termination, respectively.

[d] Estimated.

do not include instrumentation systematic errors. The averages were computed using only data with:

(1) Antenna at zenith.

(2) Clear weather.

(3) No RF spur in receiving passband.

(4) $PE_{T_{op}}D$ less than 0.1°K (from computer program).

Figure 20 shows a graph of the measurement results taken with the SPR and SRO cones operating on the 85-ft-diam DSS 13 antenna.

Some data have been taken with the SCU cone on the DSS 14 210-ft-diam antenna as a function of elevation angle (Fig. 21). It will be of interest to compare this profile with that taken when the cone is installed on the tri-cone configuration. The operating noise temperature at an elevation angle θ is related to that at zenith by

$$T_{op}(\theta) = T_{op}(90) + \left(\frac{1}{L_0} - \frac{1}{L}\right)(T_{\text{sky}} - T_{\text{cosmic}}) \quad (1)$$

where

L_0 = atmospheric loss at zenith, ratio

L = atmospheric loss at elevation angle θ, ratio

T_{sky} = "equivalent" temperature of atmosphere, °K

T_{cosmic} = cosmic noise temperature, °K

Assuming a flat earth with an atmosphere of finite height and uniform density,

$$L, \text{dB} = \frac{L_0, \text{dB}}{\sin\theta} \quad (2)$$

so that

$$L_0 = \exp\left(\frac{\ln 10}{10} L_0, \text{dB}\right) \quad (3)$$

and

$$L = \exp\left(\frac{\ln 10}{10} \frac{L_0, \text{dB}}{\sin\theta}\right) = (L_0)^{\frac{1}{\sin\theta}} \quad (4)$$

Equation (1) is shown for comparison with measurements in Fig. 21, assuming $(T_{\text{sky}} - T_{\text{cosmic}}) = 260$°K for values of zenith atmospheric loss which straddle the data. Additional data are shown in Fig. 22, indicating the small effect of azimuth on system-operating noise temperature as a function of elevation angle for DSS 14.

Table 8. Case number definition for the various cone calibration configurations

Case Number	DSS	Frequency, MHz	Cone	Configuration
1	13	2388	SPR	
2	13	2388	SRO	
3	13	2295	SRO	
4	13	2297	SCU	Cone on ground
5	14	2388	SCU	Maser 1, R&D receiver
6	14	2297	SCU	Maser 1, DSN receiver
7	14	2297	SCU	Maser 2, DSN receiver
8	14	2297	SCU	Maser 2, DSN receiver, diplexed

Table 9. Averaged system-operating noise-temperature calibrations of the various research cones operational from June 1 through October 1, 1969

Case Number	Maser gain, dB	Follow-up noise temperature contribution, °K	System-operating noise temperature, °K
1	37.9 ±0.33/0.05 (48 measurements)	0.94 ±0.09/0.01 (36 measurements)	21.3 ±0.41/0.07 (36 measurements)
2	36.7 ±1.8/0.32 (31 measurements)	0.83 ±0.08/0.01 (29 measurements)	17.1 ±0.51/0.01 (29 measurements)
3	—	0.05 ±0.02/0.01 (3 measurements)	18.8 ±0.43/0.25 (3 measurements)
4	49.1 ±0.56/0.11 (25 measurements)	0.07 ±0.01/0.00 (6 measurements)	13.1 ±1.1/0.43 (6 measurements)
5	34.6 ±0.32/0.08 (17 measurements)	2.5 ±0.53/0.16 (11 measurements)	22.6 ±0.82/0.25 (11 measurements)
6	48.0 ±0.38/0.05 (51 measurements)	1.2 ±0.91/0.13 (51 measurements)	16.9 ±0.96/0.13 (51 measurements)
7	50.0 ±0.81/0.23 (12 measurements)	0.26 ±0.23/0.07 (12 measurements)	22.1 ±0.40/0.12 (12 measurements)
8	50.1 ±0.30/0.12 (6 measurements)	0.58 ±0.31/0.13 (6 measurements)	24.6 ±5.1/2.1 (6 measurements)

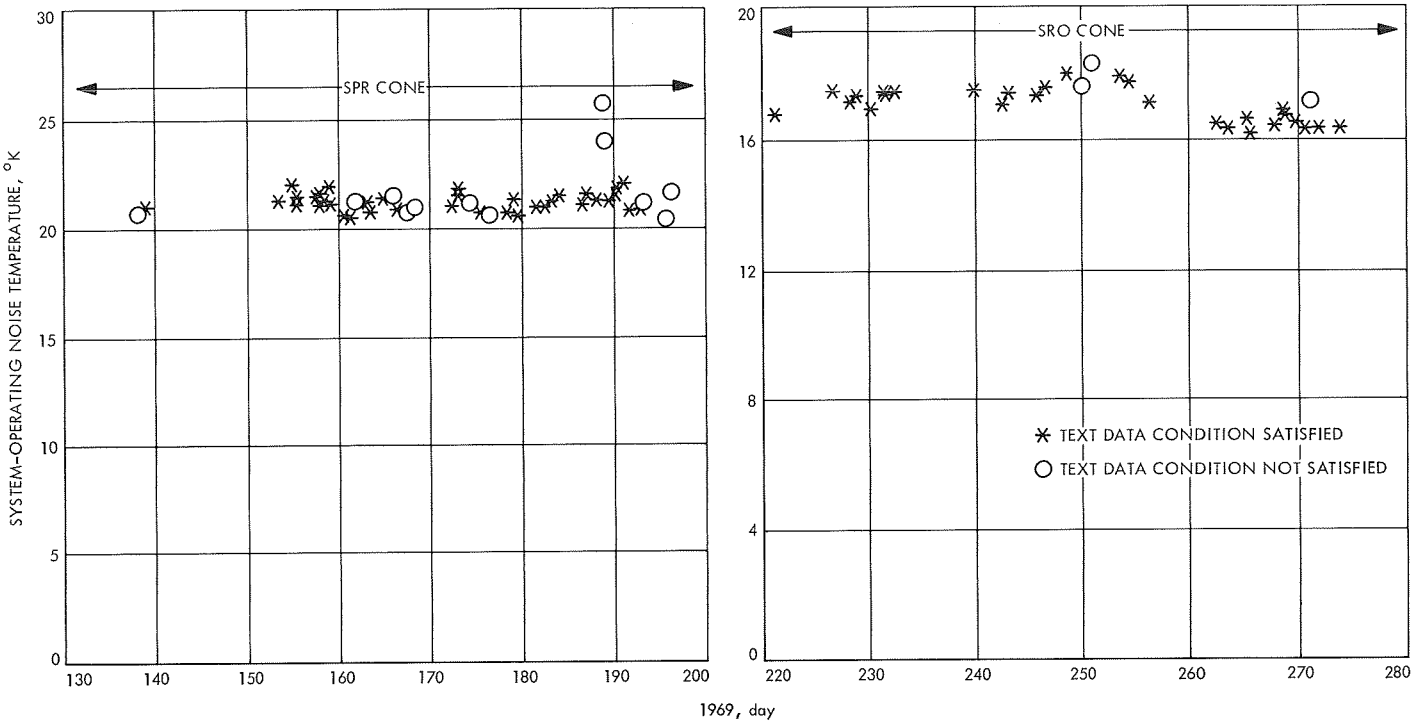

Fig. 20. System-operating noise temperature of SPR and SRO cones operational on DSS 13 antenna from June 1 through October 1, 1969

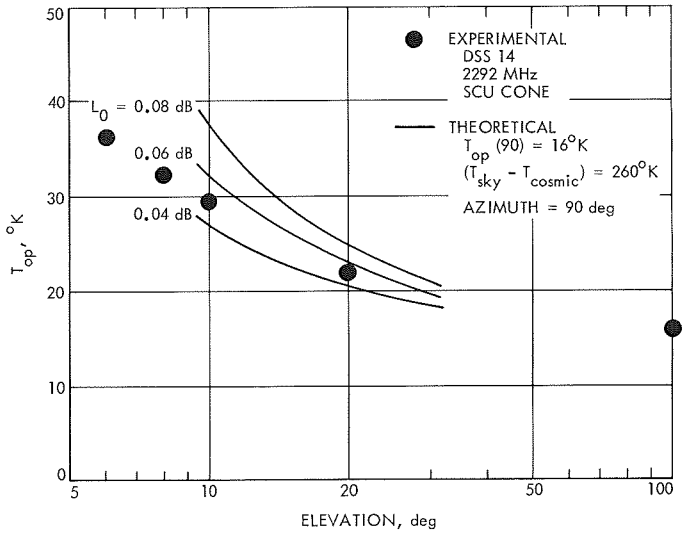

Fig. 21. System-operating noise temperature versus elevation angle for DSS 14 SCU cone (10/5/69, symmetrical mounting)

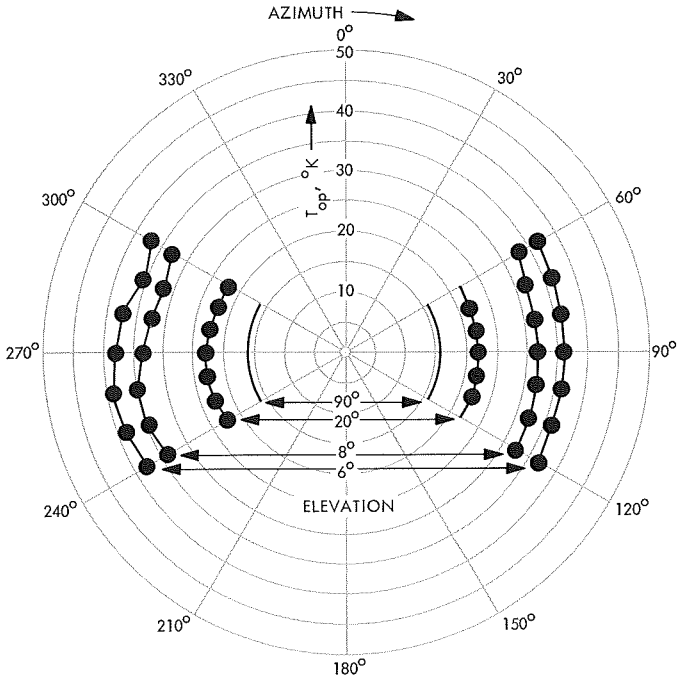

Fig. 22. System-operating noise temperature versus azimuth and elevation angles for DSS 14 SCU cone (10/5/69, symmetrical mountings)

2. Improved RF Calibration Techniques: Rotary Vane Attenuator Calibrations, T. Y. Otoshi

a. Introduction. In SPS 37-46, Vol. III, pp. 73–82, a modified theoretical attenuation law was derived for rotary vane attenuators. It is believed that precision attenuators can be made to obey the modified law up to 60 dB within tolerances of ±0.001 dB or ±0.15% of the attenuation in dB, whichever is greater. Through the use of the modified law, it should also be possible to design very short and compact rotary vane attenuators that are accurate over a 20- to 30-dB attenuation range (Ref. 1).

This article presents some preliminary results of an experimental program that was initiated to (1) test the validity of the modified law and (2) develop compact S- and X-band rotary vane attenuators for calibration of low-noise antenna systems.

b. Modified attenuation law. As derived in the referenced SPS, the modified attenuation law for rotary vane attenuators is

$$A_{dB} = -10 \log_{10} [\cos^4\theta + 10^{-L_{dB}/20} (2 \cos\phi \cos^2\theta \sin^2\theta) + 10^{-L_{dB}/10} \sin^4\theta] \quad (1)$$

where

θ = the true rotary vane angle measured relative to the plane of the vanes in the stators. (It is assumed that there is no misalignment between the vanes in the stators.)

L_{dB} = attenuation of the tangential component relative to the normal component at the rotor output, dB. (It is related to the power-loss ratio L by $L_{dB} = 10 \log_{10} L$.)

ϕ = phase-shift difference between the tangential and normal electric-field components at the rotor output, deg.

The electrical parameters L_{dB} and ϕ are unique properties of the attenuator and, hence, they must be experimentally determined for the particular attenuator being calibrated. Over a narrow frequency range, however, these parameters should essentially remain constant. Note that when L_{dB} approaches infinity, Eq. (1) will reduce to the familiar unmodified law.

For most attenuators, there will be some deviations between the indicated and true vane angle due to boresight and other readout errors. The true vane angle can be expressed as

$$\theta = \theta_I + \alpha_1 + \alpha_2 \quad (2)$$

where

θ_I = indicated vane angle

α_1 = boresight error

α_2 = angle runout error calibrated relative to $\theta_I = 0$ setting. (It is due to gearing errors, bearing runout, eccentricities, etc.)

The vane angle errors α_1 and α_2 must be calibrated to insure that the attenuator follows the law given by Eq. (1). With proper mechanical design and use of high-precision components, the angular errors α_1 and α_2 can often be made negligibly small.

c. Experimental results. To demonstrate that the modified law can be applied to improve the agreement between the actual and theoretical attenuations of a rotary vane attenuator, the results of some previous S-band calibrations (Ref. 2) were analyzed. Table 10 shows the deviations of corrected theoretical attenuations from measured attenuations. The two corrected theoretical attenuation cases shown are based, respectively, on the unmodified and modified laws; both cases include corrections made for vane angle readout errors. It can be seen that for attenuations greater than 40 dB, the agreement between measured and corrected theoretical attenuations was improved by about an order of magnitude[2] when the modified law was applied.

It should be mentioned that the values of $L_{dB} = 88$ dB and $\phi = 1.0$ deg were measured by Rantec Corp. at 2295 MHz (Ref. 3), and the measured attenuations for Table 10 were obtained by JPL at 2388 MHz. However, because the values of the parameters L_{dB} and ϕ should change only slightly over a narrow frequency range, only small errors should result if the 2295-MHz values are also used at 2388 MHz. An error analysis given in the referenced SPS and in SPS 37-46, Vol. IV, pp. 253–258, indicates that small errors in determining the values of L_{dB} and ϕ will result in only second-order-type errors on the corrected attenuations.

[2]This type of improvement may not always be possible if other errors (such as those caused by mismatch and stator vane misalignment) become significant at the higher vane-angle settings.

Table 10. Comparison of theoretical and measured attenuations for the S-band rotary vane attenuator at 2388 MHz

Indicated vane angle θ_i, deg	Apparent theoretical attenuation A_i, dB	Measured vane angle[a] θ, deg	Runout error[b] α_2, deg	Unmodified law		Modified law	
				Corrected theoretical attenuation A, dB	Deviation from measured attenuation $(A - A_m)$, dB	Corrected theoretical attenuation[c] A, dB	Deviation from measured attenuation $(A - A_m)$, dB
2.749	0.0200	2.755	0.006	0.0201	0.0004	0.0201	0.0004
3.887	0.0400	3.887	0.000	0.0400	0.0006	0.0400	0.0006
4.759	0.0600	4.761	0.002	0.0601	0.0006	0.0600	0.0005
5.495	0.0800	5.499	0.004	0.0801	0.0008	0.0801	0.0008
6.142	0.1000	6.146	0.004	0.1001	0.0008	0.1001	0.0008
8.678	0.2000	8.684	0.006	0.2003	0.0008	0.2003	0.0008
12.248	0.4000	12.258	0.010	0.4007	0.0014	0.4006	0.0013
14.972	0.6000	14.989	0.017	0.6014	0.0021	0.6013	0.0020
17.255	0.8000	17.271	0.016	0.8015	0.0026	0.8014	0.0025
19.255	1.0000	19.272	0.017	1.0018	0.0003	1.0018	0.0003
26.969	2.0000	26.987	0.018	2.0028	−0.0011	2.0027	−0.0012
32.712	3.0000	32.734	0.022	3.0043	−0.0017	3.0041	−0.0019
37.408	4.0000	37.429	0.021	4.0049	−0.0026	4.0046	−0.0029
41.419	5.0000	41.446	0.027	5.0072	−0.0016	5.0070	−0.0018
44.932	6.0000	44.964	0.032	6.0097	−0.0008	6.0093	−0.0012
48.061	7.0000	48.095	0.034	7.0115	0.0000	7.0112	−0.0003
50.879	8.0000	50.911	0.032	8.0119	−0.0006	8.0113	−0.0012
53.440	9.0000	53.476	0.036	9.0147	−0.0015	9.0140	−0.0022
55.782	10.0000	55.822	0.040	10.0178	0.0019	10.0170	0.0011
59.921	12.0000	59.955	0.034	12.0178	−0.0018	12.0166	−0.0030
63.469	14.0000	63.505	0.036	14.0219	−0.0040	14.0206	−0.0053
66.540	16.0000	66.578	0.038	16.0266	−0.0019	16.0247	−0.0038
69.218	18.0000	69.257	0.039	18.0312	−0.0006	18.0288	−0.0030
71.565	20.0000	71.607	0.042	20.0382	0.0029	20.0351	−0.0002
76.282	25.0000	76.330	0.048	25.0597	0.0021	25.0534	−0.0042
79.757	30.0000	79.799	0.042	30.0706	0.0010	30.0604	−0.0092
82.337	35.0000	82.381	0.044	35.0994	0.0064	35.0809	−0.0121
84.261	40.0000	84.306	0.045	40.1363	0.0090	40.1021	−0.0252
85.699	45.0000	85.758	0.059	45.2395	0.0829	45.1753	0.0187
86.776	50.0000	86.829	0.053	50.2877	0.1140	50.1740	0.0003
87.583	55.0000	87.632	0.049	55.3556	0.1744	55.1547	−0.0265
88.188	60.0000	88.242	0.054	60.5254	0.3265	60.1674	−0.0315

[a]Measured by the JPL Mechanical Inspection Department.

[b]$\alpha_2 = \theta - \theta_i$ because it was determined that the boresight error $\alpha_1 = 0$ deg. See Eq. (2).

[c]Experimental values of 88 dB and 1.0 deg were used for L_{dB} and ϕ, respectively.

Some experimental data have recently been obtained on a compact X-band attenuator. Preliminary measurements indicate that the short attenuator follows the modified law very closely. More data are currently being obtained.

References

1. Stelzried, C. T., Otoshi, T. Y., Nixon, D. L., *Compact Precision Rotary Vane Attenuator*, Invention Report 30-1212. Jet Propulsion Laboratory, Pasadena, Calif., Mar. 5, 1968.
2. Finnie, C. J., Schuster, D., Otoshi, T. Y., *AC Ratio Transformer Technique for Precision Insertion Loss Measurements*, Technical Report 32-690. Jet Propulsion Laboratory, Pasadena, Calif., Nov. 30, 1964.
3. *Test Report on Relative Phase Shift Measurements Performed on a Rotary Vane Attenuator*, Report 70122-FR. Rantec Corp., Calabassas, Calif., Mar. 29, 1967.

3. Improved RF Calibration Techniques: Noise Source Instrumentation at DSSs 13 and 14, *K. B. Wallace*

Low-noise receiver instrumentation usually includes some type of noise source for calibration purposes. For example, in radiometric measurements of planets and boresight measurements using radio stars, it is helpful to have a well-calibrated multi-valued noise source to bracket unknown noise temperatures. Gas tubes have been the most useful noise sources and are still in use in the DSN to calibrate system temperature measurements.

The noise-source method of system temperature measurement has been supplanted by an ambient termination technique at DSSs 13 and 14, but noise sources have not been eliminated from the systems. The aforementioned radiometric and source measurements, as well as noise-adding gain stabilization research, are reasons enough to retain noise sources.

The recent development of solid-state microwave noise sources has revived interest in the use of noise sources for calibration and has been instrumental in an improvement in overall system temperature (Fig. 23). These noise sources have several advantages compared with gas tubes. Gas tubes require high voltages to operate. The aging and failure rates require frequent calibration. The devices are relatively large and fragile and difficult to temperature-stabilize. The excess noise realizable is about 20,000°K. After injection to the receiver through several directional couplers, the usable excess noise is typically about 50°K. Noise diodes are low-voltage devices, 28 Vdc being typical. They are quite small and compact. The largest now in use is ¾ in. square by 2 in. long. Some of these units are installed in constant temperature ovens at DSS 14. No data on failure rate are yet available, but the devices are operated in a low-power dissipation mode and long life is anticipated. Stability of noise output appears as good as a well-aged gas tube, although sufficient data to define stability limits have yet to be accumulated. The excess noise available is typically about 400,000°K. Using the same couplers as for a gas-tube system, the injected noise can be as high as 1000°K. At present, there is no need for such high values of injected noise; therefore, higher-valued couplers are used. For example, a 26-dB coupler was replaced with a 33-dB coupler. This reduced total system temperature by approximately 0.5°K. The small size of the devices permits the installation of several units in a system, to provide a greater range of noise values. Noise-adding radiometric gain stabilization techniques require switching of the noise source at various rates, e.g., 8 Hz. DSS 13 and 14 instrumentation systems have been designed to accommodate this requirement. The exact needs of the experimenters are not known, so the systems have been made more flexible than required for ordinary station operation. At DSS 14, the noise diodes are in ovens, with temperature and voltage readouts. The ovens may be switched off if desired. Modulation instrumentation is provided (Fig. 24). DSS 13 is similarly instrumented, except ovens are omitted.

It was recently demonstrated at DSS 13 that noise diodes can be square-wave modulated up to at least 100 Hz (Fig. 25).

Noise source values of injected noise temperature are:

Source	Temperature (DSS 13), °K	Temperature (DSS 14), °K
High noise	45	133
Medium noise	3	11 (maser 2), 36 (maser 1)
Low noise	2	3

These values are preliminary and are subject to refinement. Limits on accuracy and stability will be provided as more data are accumulated. Voltage standing-wave ratio (VSWR) and VSWR change of noise diodes are parameters requiring investigation. Presently, available devices are not particularly good in these respects.

An evaluation program is under way to determine the capabilities and limitations of these new devices.

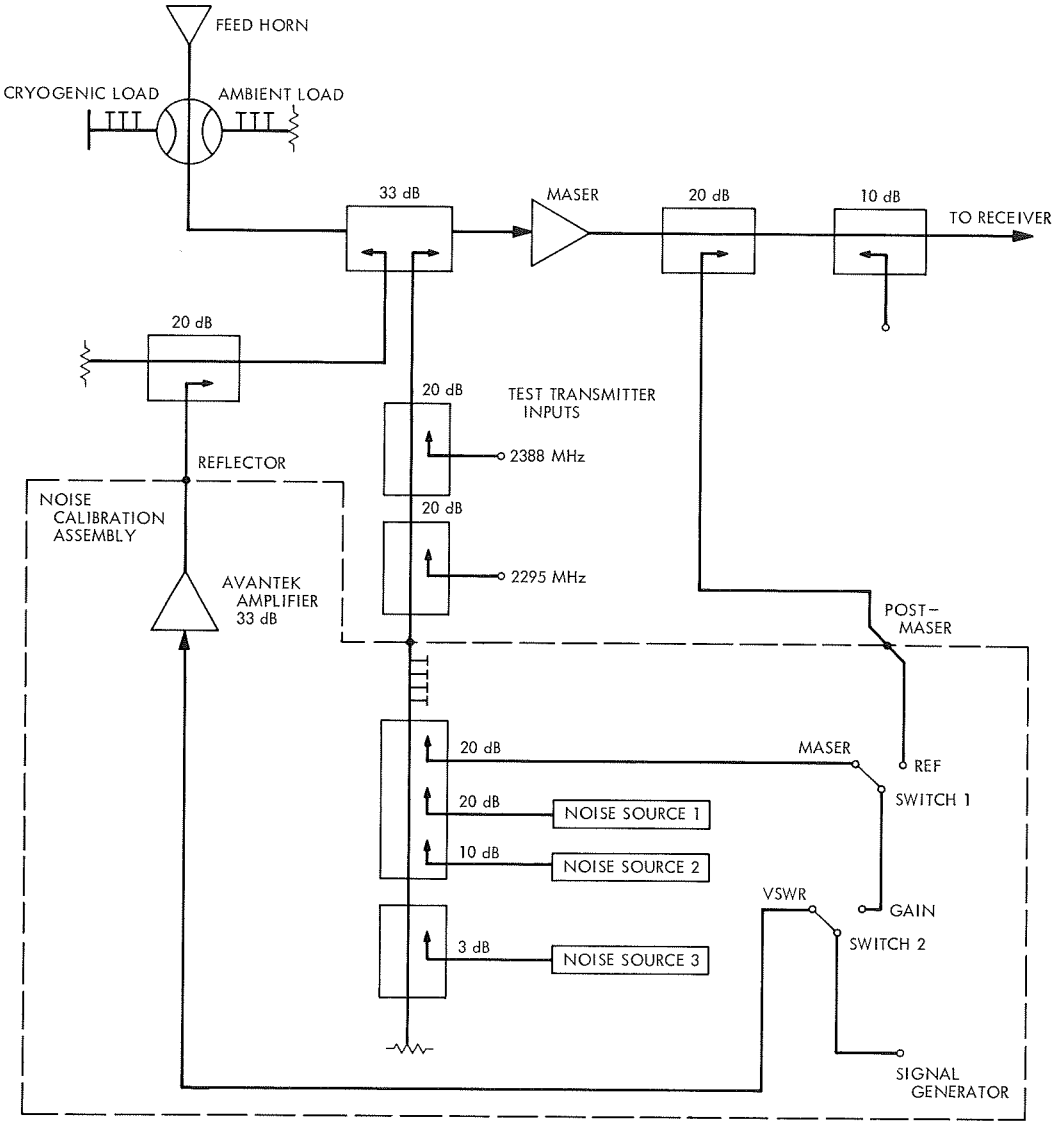

Fig. 23. Noise instrumentation of S-band cassegrain ultra cone at DSS 14

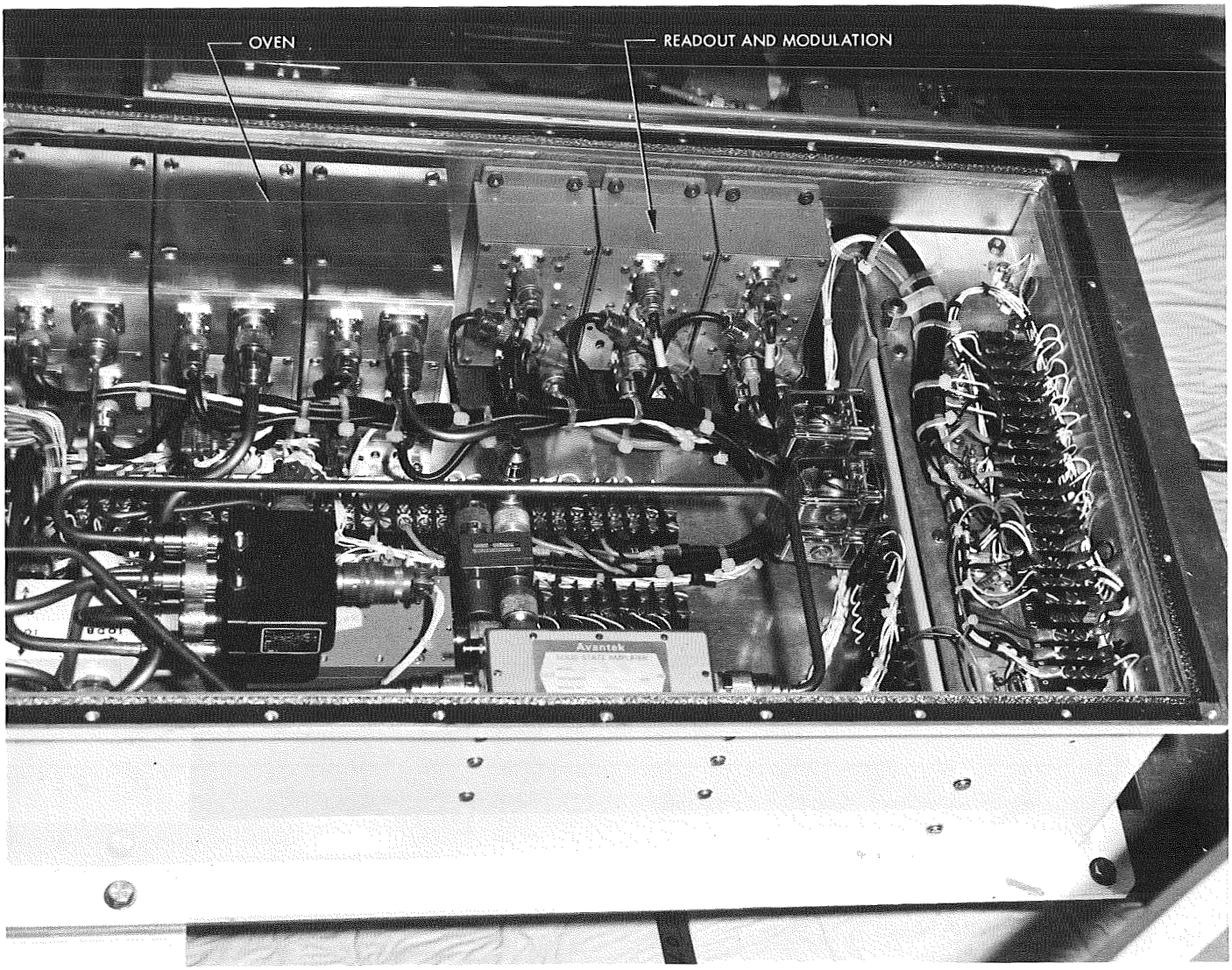

Fig. 24. Noise calibration assembly at DSS 14

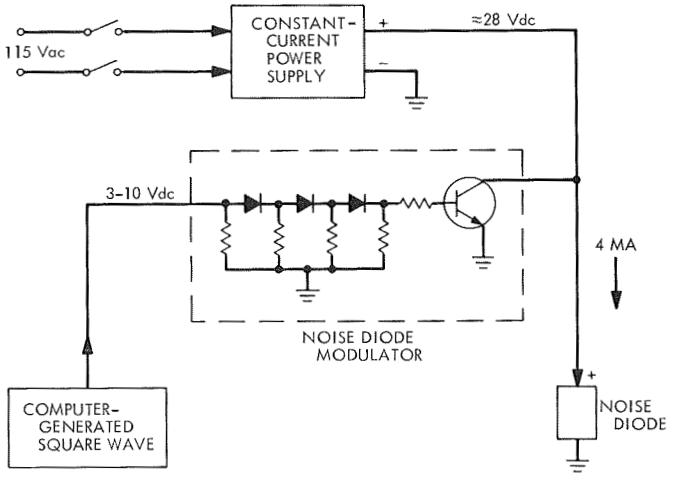

Fig. 25. Noise diode modulation